

Article

Optimization of Nanocomposite Films Based on Polyimide–MWCNTs towards Energy Storage Applications

Adriana Petronela Chiriac¹, Mariana-Dana Damaceanu¹, Mihai Asandulesa¹ , Daniela Rusu² and Irina Butnaru^{1,*}

¹ Electroactive Polymers and Plasmochemistry Department, “Petru Poni” Institute of Macromolecular Chemistry, 700487 Iași, Romania

² Physics of Polymers and Polymeric Materials, “Petru Poni” Institute of Macromolecular Chemistry, 700487 Iași, Romania

* Correspondence: butnaru.irina@icmpp.ro

Abstract: In order to obtain polyimide-based composite materials for energy storage applications, four synthetic methods towards a polyimide matrix with 2 wt.% pristine or acid-functionalized MWCNTs have been developed. The polyimide is derived from a nitrile aromatic diamine and a fluorene-containing dianhydride which allowed the formation of flexible free-standing nanocomposite films. The films were thoroughly characterized by means of structural identification, morphology, mechanical, thermal and dielectric behavior, as well as the charge storage performance. The obtained data indicated higher homogeneity of the composites loaded with acid-functionalized MWCNTs that enabled significantly increased dielectric properties compared to the matrix. To assess the electrical charge storage capability, cyclic voltammetry and galvanostatic charge–discharge measurements were employed in a three-electrode cell configuration. Due to the higher conductivity of pristine MWCNTs compared to acid-functionalized ones, increased capability to store charges was achieved by the nanocomposites containing these fillers, despite their lower homogeneity. An attempt to increase the carbonaceous material content was made by applying a thin carbon layer onto the nanocomposite film surface, which led to higher capacitance.

Keywords: nitrile-based polyimide nanocomposites; thermal properties; dielectric behavior; electrical charge storage capability



Citation: Chiriac, A.P.; Damaceanu, M.-D.; Asandulesa, M.; Rusu, D.; Butnaru, I. Optimization of Nanocomposite Films Based on Polyimide–MWCNTs towards Energy Storage Applications. *Energies* **2023**, *16*, 3739. <https://doi.org/10.3390/en16093739>

Academic Editor: Antonino S. Aricò

Received: 20 March 2023

Revised: 19 April 2023

Accepted: 25 April 2023

Published: 27 April 2023



Copyright: © 2023 by the authors. Licensee MDPI, Basel, Switzerland. This article is an open access article distributed under the terms and conditions of the Creative Commons Attribution (CC BY) license (<https://creativecommons.org/licenses/by/4.0/>).

1. Introduction

The development of sustainable and clean energy requires the improvement of energy-storage devices able to deliver fast/ultrafast fully charging/discharging and much higher power delivery (>10 kW/kg) for shorter periods of time [1]. In this respect, supercapacitors have gained an increasing interest since they are able to integrate interfacial adsorption and redox reactions, hierarchical microstructures, conductivity, mechanical strength and flexibility towards high power intensity and long lifetime [2–5]. Carbonaceous materials [6,7], especially carbon nanotubes (CNTs), have been fervently used as electrode materials in supercapacitors due to their excellent physical and chemical properties [8]. CNTs display high conductivity, a highly accessible outer surface, unique pore structure, elevated mechanical strength and thermal stability. Usually, CNTs cannot be used in their bulk form due to the poor translation of individual CNTs’ characteristics into their macroscopic forms. Thus, the applications of CNTs often imply their strategic combination with polymers, which leads to the development of new materials with enhanced features with regard to mechanical resistance, thermal stability and electrical conductivity, as well as increased impact and tribological characteristics, depending on the dimension of the fillers and the matrix’s dispersion ability [9]. Some drawbacks of CNTs such as moderate level of specific surface area and the packing density need to be improved considering areal/volumetric

performances [1,10]. Still, the choice of adding CNTs into a polymer matrix leads to the formation of advanced nanocomposites, which show an increased, or sometimes, completely new electrical, thermal, mechanical, electrochemical or electromagnetic properties, making CNTs-based materials attractive candidates for supercapacitor electrode applications, such as conducting additives, templates/scaffolds for nanocomposite electrodes and platforms for flexible/stretchable devices, among others [2–5].

From the polymer matrix point of view, there is an increasing need for high-insulating polymers that are easily processable and compatible with high-permittivity nanoparticles. Since the dielectric constant values for organic and non-ferroelectric polymers are in the range of 2–4 [11], new polymers have been developed for the electronics industry. The most suitable polymers for plastic substrates which fulfill the requirements of the industry are polyimides, polybenzoxazoles, polybenzimidazoles and polybenzthiazoles. Aromatic polyimides (PI) are widely known as high-performance polymers convenient for advanced electric and microelectronic devices due to their straightforward synthesis, very good electric insulation properties, inherent flame-retardant properties, long-term heat resistance and high glass transition temperatures [12–14]. However, when polyimide chain structures are adequately modified, high-k polymer films can be obtained. It was demonstrated that the incorporation of nitrile units in PI chains leads to the increase in dielectric constant value [15–21], while it enables the PI adhesion to many substrates, most likely due to the polar and hydrogen bonding interactions with the surface groups that contain oxygen or hydroxy units [22]. In addition, since the nitrile group is usually directly grafted on the aromatic core, the polyimides will maintain their inherent high thermal stability [23,24].

Versatile CNTs–PI nanocomposites have been developed so far by using the synergetic combination of polyimides (which possess high mechanical, electrical, thermal, optical and/or electrochemical features) with the excellent features of CNTs (including high mechanical, electrical, thermal and magnetic properties, chemical stability and high aspect ratio) [25]. The materials based on homogeneous CNTs–polyimide composites are expected to possess overall improved physical properties of the pristine polymer matrix, thereby extending their field of applications. However, for a homogeneous dispersion of CNTs into PI matrix, chemical or physical modifications have been performed on both polyimide and CNTs to attain the desired characteristics required by high-tech fields of industry. The most used procedures for CNTs modifications consist in acid or amino functionalization [26], free-radical grafting [27], plasma treatment [28], microwave irradiation [29], or surfactants assistance [30]. Still, there are several disadvantages of these procedures since these might sacrifice some important composite properties, such as mechanical strength and electrical conductivity. The PI chains' modification involved the incorporation of functional groups or addition of aromatic rings in the molecular structure able to develop interactions with CNTs that enabled polymer wrapping onto CNTs [31], as well as polymerization of monomers covalently bonded to CNTs [32]. On the other hand, to obtain homogeneous PI–CNTs composites, a series of procedures was established for the synthesis steps, including mixing MWCNTs with the polymer in solution, melt mixing of the two components and in situ polymerization of the monomers in the presence of the fillers.

Therefore, particular applications of polyimide–CNTs composites were developed during the last decade, such as energy-related devices in lithium-ion batteries [33], micro-supercapacitors [31,34], multi-role thermal film devices [35], electromagnetic interference shielding applications [36], voltametric sensors for paracetamol detection [37], separation membranes for organic solvent nanofiltration [38], flexible pressure sensors [39] and hydrogen evolution electrocatalysts [40], among others.

As far as we know, nanocomposites obtained from nitrile-based polyimide matrices and CNTs were developed to investigate them in all-organic actuators [41] or as polymeric materials in sensors and actuators for high-temperature applications such as PI/SWCNT/lead zirconate titanate formulations [42,43] with no attempt until now to investigate them in energy storage devices, such as supercapacitors. Therefore, we considered it

of particular interest to explore the electrical charge storage capacity of flexible electrodes prepared from such PI/CNTs-based nanocomposites.

Thus, herein we report a systematic study of nanocomposite films based on nitrile-containing polyimide and pristine or acid-functionalized MWCNTs with a special concern for their performances as flexible electrode materials. The polyimide used as matrix was modified by incorporating nitrile, ether and bulky fluorene as structural elements so as to attain processability into tough films and high dielectric constant, while maintaining the high thermal stability specific for this class of polymers. For the nanocomposite synthesis, we have approached four pathways in order to explore the suitability of each method towards homogeneous composite formation and the best characteristics in terms of thermal stability, mechanical strength and dielectric behavior. Based on these, the most performant composites were selected and tested by electrochemical methods as flexible energy storage electrode materials.

2. Experimental Section

2.1. Materials

m-Aminophenol (98%), 2,6-dichlorobenzonitrile (97%), 9,9-bis(*p*-hydroxyphenyl)fluorene (97%), 4-nitrophthalonitrile (97%), multi-wall carbon nanotubes (MWCNTs, L = 6–9 mm × 5 μm, >95%), tetrabutylammonium perchlorate (TBAP, ACS reagent 98%), potassium chloride (KCl, ACS reagent), lithium perchlorate (LiClO₄, ACS reagent, ≥95.0%), sulfuric acid (ACS reagent, 95.0–98.0%) and nitric acid (ACS reagent, 70%) were purchased from Sigma-Aldrich and used without purification. A 30% carbon conductive paint was provided from MJ Chemicals, Tangerang, Indonesia. *N*-methyl pyrrolidinone (NMP, anhydrous, 99.5%), *N,N'*-dimethylformamide (DMF, HPLC grade), *N,N'*-dimethylacetamide (DMAc, HPLC grade), dimethyl sulfoxide (DMSO anhydrous, ≥99.9%), tetrahydrofuran (THF, anhydrous, ≥99.9%), acetonitrile (ACN, anhydrous, 99.8%), chloroform (anhydrous, 99%) and ethanol (analytical standard) were bought from Sigma-Aldrich and used without purification.

2.2. Synthesis

Multi-wall carbon nanotubes functionalized with carboxylic groups (MWCNTs-COOH) were obtained, as previously reported [44], by treating pristine MWCNTs with a mixture of H₂SO₄ and HNO₃ (3:2 weight ratio) in a weight ratio of mixed acids (H₂SO₄ and HNO₃):MWCNTs = 400:1. The reaction mixture was stirred at 50 °C for 24 h, after which the obtained MWCNTs-COOH were separated by centrifugation and washed thoroughly with deionized water until a neutral pH and dried in an oven for 12 h at 120 °C.

The aromatic diamine 2,6-bis(3-amino-phenoxy)benzonitrile was obtained by the nucleophilic displacement of 2,6-dichlorobenzonitrile with *m*-aminophenol in NMP, as reported earlier [24]. M.p. = 136–138 °C.

FTIR (KBr, cm⁻¹): 3465–3378 (–NH₂ stretching), 3083–3018 (–CH aromatic stretching), 2232 (–CN stretching), 1627 (aromatic C–C stretching), 1574 (NH bending), 1242 (Ar–O–Ar stretching), 773 (NH₂ out-of-plane).

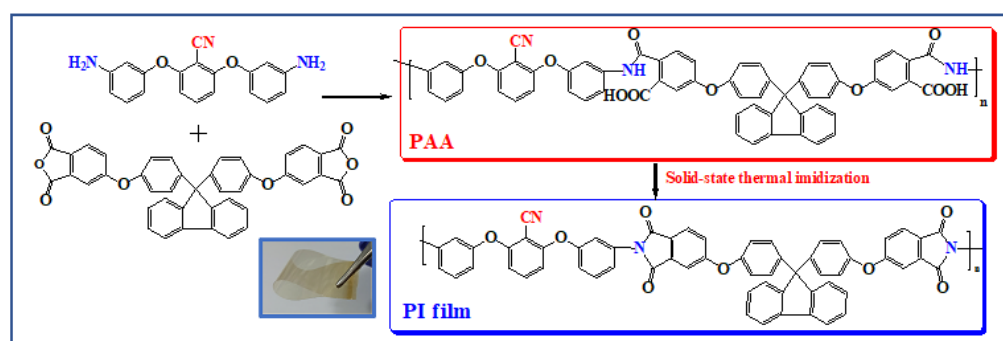
¹H-NMR (DMSO-d₆), δ (ppm): 7.55–7.50 (t, 1H), 7.10–7.06 (t, 2H), 6.60–6.58 (d, 2H), 6.46–6.44 (dd, 2H), 6.31–6.30 (t, 2H), 6.28–6.26 (dd, 2H), 5.39 (s, 4H, –NH₂). η = 80%.

The aromatic dianhydride 9,9-bis[4-(3,4-dicarboxyphenoxy)-phenyl]fluorene was synthesized by a multistep reaction, according to a published pathway [45,46]. Briefly, 4-nitrophthalonitrile was allowed to react with 9,9-bis(*p*-hydroxyphenyl)fluorene in the presence of potassium carbonate, using dimethylformamide (DMF) as solvent to obtain a tetranitrile derivative that was further hydrolyzed in alkaline solution to the corresponding tetracarboxylic acid. The final product was obtained by dehydration of the tetracarboxylic acid in the presence of acetic anhydride; M.p. = 255–257 °C.

FTIR (KBr, cm⁻¹): 3065–3039 (C–H aromatic), 1850 (C=O asymmetric), 1777 (C=O symmetric), 1618 (C=O aromatic), 1279 (C–O–C).

¹H-NMR (DMSO-d₆, ppm): 8.06 (d, 2H), 7.99–7.96(m, 2H), 7.55 (d, 2H), 7.51–7.48 (dd, 2H), 7.46–7.44 (m, 4H), 7.40–7.37 (t, 2H), 7.30–7.28 (d, 4H), 7.15–7.13 (d, 4H). η = 78.43%.

The synthetic route to nitrile-containing polyimide (PI) can be described as follows: in a 100 mL three-necked flask fitted with a nitrogen inlet and outlet, 1.352 g (0.00426 mol) of 2,6-bis(*m*-aminophenoxy)benzotrile and 15 mL of DMAc were added. After that, 2.751 g (0.00426 mol) of 9,9-bis[4-(3,4-dicarboxyphenoxy)-phenyl]fluorene and another 15 mL of DMAc were added to the flask so as to obtain a solution with a solid content of 12%. A light-brown clear solution of polyamidic acid (PAA) was obtained in the first step, which was stirred at room temperature for 21 h under a stream of nitrogen. The PAA solution was poured into methanol, filtered and washed several times with methanol to give a solid which was dried at 100 °C for 6 h. To obtain the polyimide matrix, an appropriate quantity of PAA solid was dissolved in DMAc so as to attain a solution concentration of 12%. This solution was filtered and cast onto clean glass substrates, being further subjected to a gradual solid-state thermal imidization process at 50, 75, 100, 125, 150, 175, 200 and 250 °C, each temperature for 1 h and at 300 °C for 2 h (Scheme 1). The resulting PI film had a strong adhesion to the glass support and was stripped off the plate by immersion in water. After that, the film having the thickness of about 45 µm was dried in a vacuum oven at 120 °C for 6 h and used afterwards for various studies.



Scheme 1. Pathway towards polyimide synthesis.

FTIR (ATR, cm^{-1}): 3067 (C–H aromatic), 2231 (C \equiv N stretching), 1778 (C=O imide asymmetric stretching), 1719 (C=O imide symmetric stretching), 1599 (C=C aromatic), 1367 (C–N stretching), 1240 (Ar–O–Ar stretching), 742 (C–N ring deformation).

$^1\text{H-NMR}$ (DMSO- d_6 , ppm): 7.91 (s, 4H), 7.58–7.50 (d, 5H), 7.33–7.25 (d, 18H), 7.07 (s, 4H), 6.72 (s, 2H).

2.3. Preparation of Polyimide-MWCNTs Composite Films

In order to establish the most suitable conditions towards homogeneous dispersion of MWCNTs into the selected PI matrix, four methods were approached (Scheme 2), either by using PAA powder and 2 wt.% MWCNTs-COOH or pristine MWCNTs (methods A, B and D), or by monomer polymerization in the presence of 2 wt.% MWCNTs-COOH or pristine MWCNTs (method C), as follows:

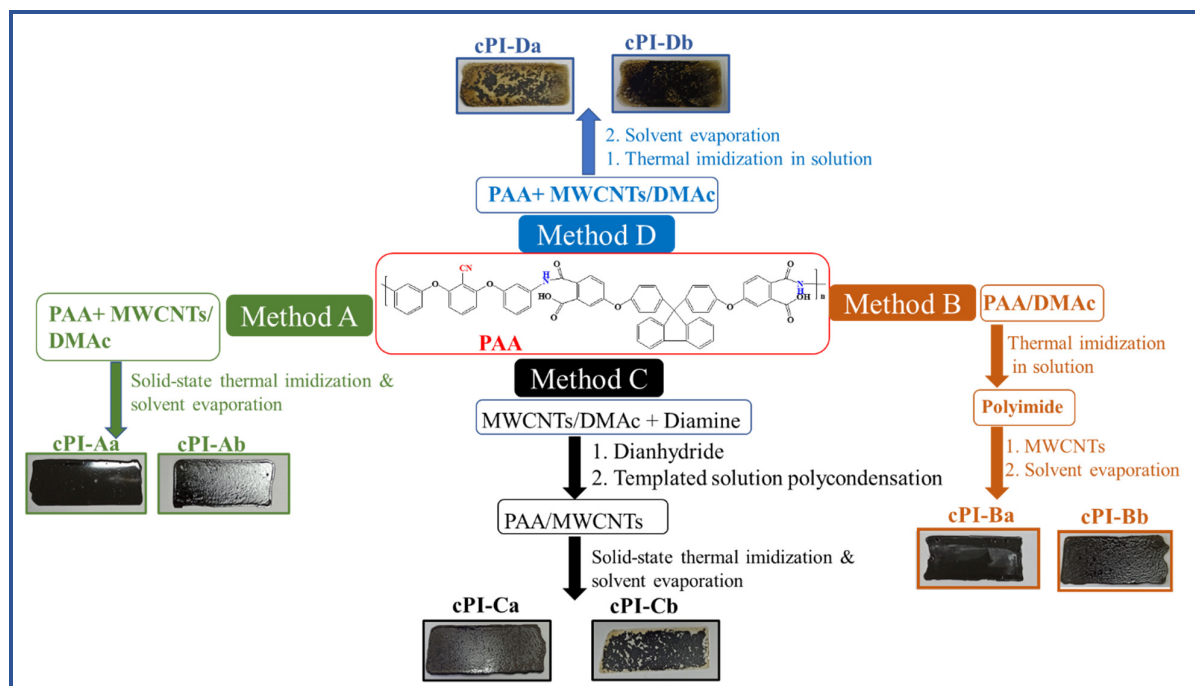
Method A: appropriate quantities of PAA powder (0.15 g) and 2 wt.% MWCNTs-COOH (0.003 g) or pristine MWCNTs (0.003 g) were mixed in 1.1 mL DMAc to obtain a suspension having 12 wt.% solids, which was then stirred at room temperature for 1 h and sonicated for another 2 h. The obtained mixture was cast onto clean glass plates and subjected to the solid-state thermal imidization procedure as described for the polyimide matrix. The sample containing 2 wt.% MWCNTs-COOH was denoted as **cPI-Aa**, while the film incorporating 2 wt.% pristine MWCNTs was noted as **cPI-Ab**. The obtained films with the thickness of about 50 µm for **cPI-Aa** and 90 µm for **cPI-Ab** were used afterwards for various studies.

Method B: appropriate quantities of PAA powder (0.3 g) and 2.2 mL DMAc were mixed in order to obtain a clear PAA solution of 12 wt.%, which was subjected to thermal imidization in solution at 165 °C for 2 h under a strong stream of nitrogen in order to remove the water formed during the cyclodehydration process. After cooling to room temperature,

half of the obtained polyimide solution was mixed with 2 wt.% MWCNTs-COOH (0.003 g) and the other part with 2 wt.% pristine MWCNTs (0.003 g), stirred at room temperature for 1 h, sonicated for 2 h and cast onto clean glass plates. The removal of the solvent and the complete imidization process was accomplished by using the same temperature regime as described for the polyimide matrix film preparation. The films obtained by this method containing 2 wt.% MWCNTs-COOH or pristine MWCNTs were denoted as **cPI-Ba** (thickness of about 50 μm) and **cPI-Bb** (thickness of about 92 μm), respectively.

Method C: Appropriate amounts of 2 wt.% MWCNTs-COOH (0.0027 g) or 2 wt.% pristine MWCNTs (0.0027 g) were mixed with 1 mL DMAc and sonicated for 30 min. To this solution, equimolar quantities of 2,6-bis(m-aminophenoxy)benzotrile (0.045 g) and 9,9-bis[4-(3,4-dicarboxyphenoxy)-phenyl]fluorene (0.09 g) were added to obtain mixtures of 12 wt.% solids, each monomer addition being followed by sonication for 15 min. These mixtures were stirred afterwards at room temperature for 2 h under a stream of nitrogen and then cast onto clean glass plates. The solid-state cyclodehydration of PAA to the corresponding PI was performed by following the same programmed thermal treatment as the one applied for the PI film matrix. The composite film containing 2 wt.% MWCNTs-COOH was denoted as **cPI-Ca** (thickness of about 51 μm), while the film incorporating 2 wt.% pristine MWCNTs was denoted as **cPI-Cb** (thickness of about 56 μm).

Method D: appropriate quantities of PAA powder (0.15 g) and 2 wt.% MWCNTs-COOH (0.003 g) or pristine MWCNTs (0.003 g) were mixed in 1.1 mL DMAc under ultrasonication for 15 min to obtain a suspension with 12 wt.% solids content, which was further subjected to a thermal treatment at 165 $^{\circ}\text{C}$ for 2 h under a strong stream of nitrogen to perform the imidization of PAA. After cooling, the solution mixture was sonicated for 2 h and cast onto clean glass plates. To remove the solvent and to complete the imidization process, the films followed the same temperature regime as described for the polyimide film matrix. The obtained films were denoted as **cPI-Da** (the sample with 2 wt.% MWCNTs-COOH, thickness of about 60 μm) and **cPI-Db** (the sample incorporating 2 wt.% pristine MWCNTs, thickness of about 80 μm).



Scheme 2. Synthetic approaches to obtain polyimide composites with 2 wt.% MWCNTs and pictures of the corresponding composites.

2.4. Measurements

Fourier-transform infrared spectroscopy (FTIR) measurements were performed on a FT-IR Bruker Vertex 70 Spectrophotometer in the ATR mode by using strips of free-standing films.

^1H NMR spectra were carried out with a Bruker Avance III 400 spectrometer, operating at 400 MHz. The chemical shifts are expressed in δ units (ppm) with respect to the residual peak of the solvent DMSO- d_6 : 2.512 ppm.

The morphology of the polyimide–MWCNT films was evaluated by using a Verios G4 UC Scanning Electron Microscope (SEM) from Thermo Fisher Scientific equipped with an energy dispersive spectrometer (EDS, EDAX Octane Elite). The samples were broken in liquid nitrogen and were sputtered with Pt in order to analyze the fracture section.

The optical microscopy photographs were taken by using an Olympus BH-2 polarized light microscope at a magnification of 40x.

The thermal stability of the films was evaluated by thermogravimetric analysis (TGA), which was performed on a Thermogravimetric Analyzer, Discovery TGA 5500, under nitrogen flow ($20\text{ cm}^3/\text{min}$), at a heating rate of $10\text{ }^\circ\text{C}/\text{min}$, from 25 to $700\text{ }^\circ\text{C}$.

The glass transition temperature of the films was performed with a Differential Scanning Calorimeter, Discovery DSC 250 apparatus, in the temperature window from 25 to $300\text{ }^\circ\text{C}$.

The mechanical tests were made on a Shimadzu AGS-J deformation apparatus. The deformation rate was $1\text{ mm}/\text{min}$, with a load cell able to measure forces up to 1 kN . The free-standing film samples had an area of $20 \times 5\text{ mm}$ and were subjected to tensile tests at room temperature. For each data point, three samples were tested and the average value was calculated.

Broadband Dielectric Spectroscopy (BDS) measurements were performed by using a Novocontrol Concept 40 Broadband Dielectric Spectrometer equipped with an Alpha-A frequency analyzer and a Quatro Cryosystem device for the control of temperature. The free-standing films were placed between two round plate electrodes (provided by Novocontrol) and then mounted in the BDS active sample cell. The dielectric parameters were collected isothermally in a frequency window between 100 Hz and 10^6 Hz and at temperatures between $-100\text{ }^\circ\text{C}$ and $250\text{ }^\circ\text{C}$. Previous to dielectric measurements, the samples were heated up to $200\text{ }^\circ\text{C}$ in order to eliminate the thermal history. The dielectric measurements were performed on a PI matrix and relevant polyimide-based nanocomposites. Thus, the dielectric spectra of nanocomposites based on pristine, non-functionalized MWCNTs (**cPI-Ab**, **cPI-Bb**, **cPI-Cb**, **cPI-Db**) could not be adequately recorded due to the non-homogeneous distribution of MWCNTs in the PI matrix.

Cyclic voltammetry (CV) measurements were registered on a Potentiostat-Galvanostat (PG581, Uniscan Instruments, Buxton, UK). Galvanostatic charge-discharge (GCD) curves were recorded with the same equipment by means of chronopotentiometry experiments. The electrochemical cell was equipped with three electrodes: a reference electrode (Ag/Ag^+), an auxiliary electrode (platinum wire) and a working electrode (the cPI free-standing film welded with a silver wire). A 5 M KCl aqueous solution or 0.1 M lithium perchlorate (LiClO_4)/tetrabutylammonium perchlorate (TBAP)/acetonitrile (ACN) were used as supporting electrolytes. Prior to any measurement, the electrochemical cell was purged with a gentle nitrogen flow.

3. Results and Discussion

The present study aims to establish the most efficient way towards development of homogeneous composite CN-functionalized polyimide materials endowed with high thermal, mechanical and dielectric properties that are suitable for use in flexible energy storage devices. Thus, a special interest arose in the evaluation of the polar nitrile unit's influence on the physico-chemical properties of the polyimide composites, being known that it develops hydrogen bonds with the groups containing $-\text{O}$ or $-\text{OH}$ units [22]. For this purpose, several strategies were approached, either by using two types of MWCNT fillers

(pristine or acid-functionalized) and four methods for the polyimide-composite synthetic pathway. The nature of the MWCNTs may influence the filler dispersion homogeneity; for instance, COOH-functionalized MWCNTs can lead to better interaction of the fillers with the polyimide matrix by hydrogen bond formation in addition to π - π interaction between the aromatic rings belonging to both MWCNTs and polyimides.

Among the selected synthetic procedures, three methods (A, B and D) were based on the processing from the PAA precursor stage, previously obtained from an aromatic diamine containing polar nitrile and ether groups and a dianhydride incorporating ether and bulky pendant fluorene units. Method C differs from the other three pathways in terms of a different synthetic approach which does not involve the PAA but the filler-templated polycondensation reaction. There are certain similarities between methods B and D (in terms of polyimide composite film formation) since both films were cast from the polyimide solution, except that **cPI-D** films were obtained by imidization in the presence of MWCNT fillers, while in the case of **cPI-B** films, MWCNTs were introduced in the polyimide solution after the thermal treatment had finished. When methods A and C were applied, the composite films were processed from the intermediary PAA solution by solid-state imidization. Thus, **cPI-C** films were obtained by templated polymerization of the monomers (in the presence of MWCNTs) and solid-state thermal treatment of the resulting PAA/MWCNTs composites, unlike the preparation of **cPI-A** films where MWCNTs were introduced in the already obtained PAA solution that was further subjected to the imidization process.

3.1. Physico-Chemical Characterization

The synergism of different structural elements incorporated into this novel PI architecture endowed the macromolecular chains with good solubility at room temperature in polar aprotic solvents such as NMP, DMAc or DMSO. This solubility can be mainly attributed to the presence of flexible ether groups along the main chain coming from both starting monomers and to the bulky pendant fluorene unit. The cumulative effect of these moieties enabled the decrease in the macromolecular rigidity and molecular packing into thigh structure, allowing solvent-solute interactions and solution-processing of the resulting PI.

The good solubility of PI in DMSO allowed structural identification by $^1\text{H-NMR}$ spectroscopy. $^1\text{H-NMR}$ spectra confirmed the complete cyclodehydration process of the intermediary PAA to the fully cyclized polyimide form by the absence in the PI $^1\text{H-NMR}$ spectrum of the signals associated with the amide and carboxylic acids protons, which were identified in the PAA spectrum (Figure 1) at approx. 10.53 ppm and 13.01 ppm (as a broad band), respectively. The other aromatic protons of the main chain were found according to the influence of the electron effects of their surrounding structural elements: signals at the lowest resonance field (7.91 and 7.33 ppm) were correlated with the protons of the dianhydride fragment, which induced deshielding due to the electron-withdrawing effect of the phthalimide cycle. The groups of signals found at slightly lower shifts, 7.58, 7.07 and 6.72 ppm, were associated with the aromatic protons of the CN-based aromatic diamine segment since the polar CN group also withdrew electrons from the polymer structures.

The PI structure was further confirmed by FTIR spectroscopy by the presence of the characteristic newly formed imide absorption bands attributed to asymmetrical and symmetrical stretching of C=O units at 1778 and 1719 cm^{-1} , respectively, and C-N linkage imide vibration at 1367 cm^{-1} , while the imide ring deformation was observed at 742 cm^{-1} . The nitrile unit was identified at 2231 cm^{-1} , while the aromatic ether unit was found at 1238 cm^{-1} . Since the structural design of the polyimide matrix is identical for all composite films, their FTIR spectra displayed comparable features. Still, small shifts of about 2–6 cm^{-1} and significant band broadening of the absorption band characteristics for the functional groups of the composites are a proof of the specific interaction of MWCNTs with aromatic nuclei and ether units of the polyimide matrix. Figure 2 is an illustrative example of the FTIR spectrum of the PI matrix, **cPI-Ba** and **cPI-Bb**. Thus, FTIR spectra of composite films showed the same characteristic bands as the one found in PI, with several small red shifts

and significant absorption band broadening which occurred due to imide C=O absorption (from 1778 to 1776 cm^{-1} and from 1719 to 1717–1716 cm^{-1}), C=C aromatic stretching (from 1599 to 1594–1593 cm^{-1} and from 1496 to 1484–1482 cm^{-1}), C–N linkage (from 1367 to 1365–1363 cm^{-1}) and imide ring deformation (from 742 to 738–734 cm^{-1}), confirming the interaction of the conjugated graphene-like surface of MWCNTs with the aromatic PI matrix (Figure 2b,c).

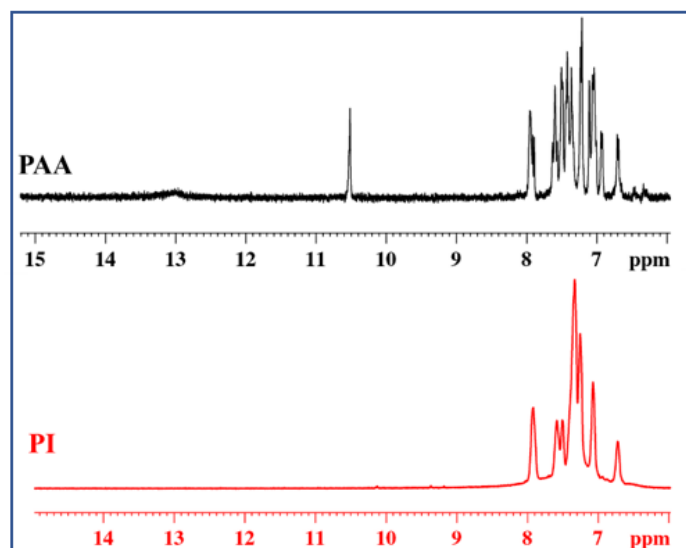


Figure 1. Comparative ^1H -NMR spectra of PAA and of the corresponding PI.

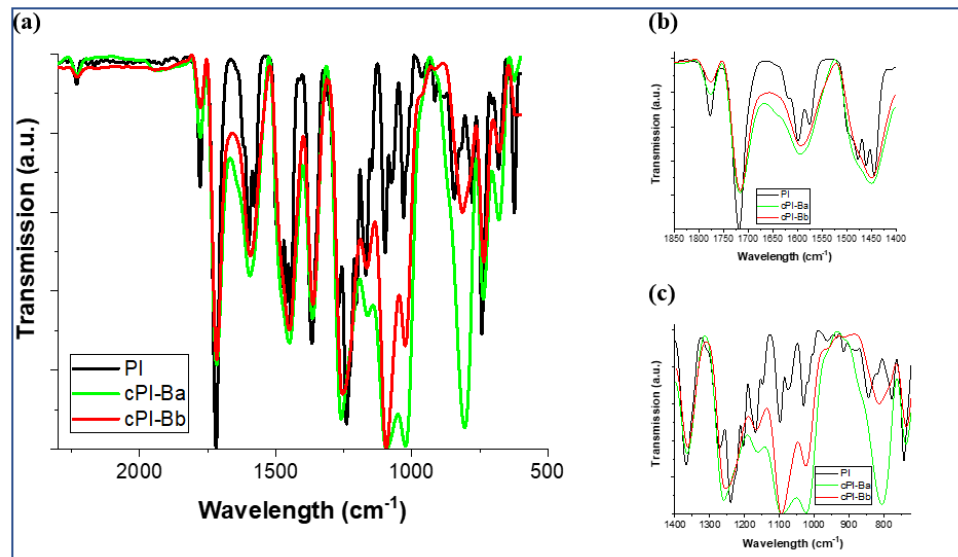


Figure 2. (a) FTIR spectra of PI, cPI-Ba and cPI-Bb. Enlarged FTIR spectra of PI, cPI-Ba and cPI-Bb in the regions (b) 1800–1400 cm^{-1} and (c) 1400–720 cm^{-1} .

Any attempt to record Raman spectra on the composite films failed since the PI matrix exhibited inherent fluorescence that impeded obtaining conclusive information on the structure of MWCNTs dispersed in the PI matrix.

3.2. Morphology Studies

The visual observation of the composite films enabled a first deduction on the efficiency of mixing by each employed method to obtain the CN-substituted PI materials. As can be observed from Figure 3, methods A, B and C (films cPI-Aa, cPI-Ab, cPI-Ba, cPI-Bb

and **cPI-Ca**) seem to be more efficient towards homogeneous PI/MWCNTs film formation, except method C where pristine MWCNTs were used (film **cPI-Cb**). To support visual observations, optical microscopy (OM) photographs were recorded at a magnification of 40× (Figure S1) that provided additional support for the nature of MWCNTs' dispersion in the polyimide matrix. Accordingly, the composite films obtained by methods A and B regardless of MWCNTs type and by method C by using acid-functionalized MWCNTs were homogeneous. Although it was expected that CN units from the PI matrix would develop hydrogen bonds with MWCNT fillers, this phenomenon was not observed, a homogeneous dispersion being mainly found in composite films based on COOH-functionalized fillers, except those obtained by method D, as shown in Figure 3 (films **cPI-Da** and **cPI-Db**). Thus, the composite films **cPI-Aa**, **cPI-Ba** and **cPI-Ca**, after solvent removal, displayed a surface uniformly covered by the nanotubes. This is in line with the thickness of the composite films (Table 1), which registered higher values for the films containing pristine MWCNTs. The pristine MWCNTs tend to protuberate out of the polymer matrix, leading to higher thicknesses and rougher surfaces of the films, although they have the same processing method from suspensions with identical MWCNT content and PI solution concentration as the samples containing functionalized fillers.

Table 1. Mechanical and thermal properties of PI matrix and composite films containing 2 wt.% MWCNTs.

Sample	Tensile Strength [MPa]	Elongation at Break [%]	Young's Modulus [GPa]	Φ [μm]	T_g [$^{\circ}\text{C}$]	T_5 [$^{\circ}\text{C}$]	T_{max} [$^{\circ}\text{C}$]	W_{700} [%]
PI	95.38 ± 2.1	9.45 ± 0.9	1.49 ± 0.7	45	240	526	550/620	65.16
cPI-Aa	53.36 ± 0.8	7.55 ± 0.2	0.91 ± 0.4	50	243	546	560/620	69.62
cPI-Ab	71.31 ± 1.2	8.75 ± 0.7	1.29 ± 0.8	90	241	537	560/620	70.99
cPI-Ba	58.22 ± 4.4	5.85 ± 0.8	1.12 ± 1.5	50	240	540	560/ *	69.17
cPI-Bb	39.79 ± 3.2	6.33 ± 0.6	0.96 ± 2.0	92	240	534	560/610	69.51
cPI-Ca	36.84 ± 2.3	5.71 ± 0.4	0.91 ± 0.3	51	240	544	565/ *	68.88
cPI-Cb	44.39 ± 2.1	6.09 ± 0.4	0.97 ± 1.5	56	240	530	565/612	68.68
cPI-Da	46.54 ± 2.2	6.29 ± 0.1	1.01 ± 0.9	60	240	534	565/620	66.92
cPI-Db	44.27 ± 7.5	7.98 ± 0.9	0.86 ± 0.4	80	240	530	565/610	69.75

Φ = film thickness; T_g = glass transition temperature; T_5 = temperature of 5% weight loss; T_{max} = maximum decomposition temperature; W_{700} = char residue at 700 $^{\circ}\text{C}$; * broad band with no clear peak.

In order to further evaluate the dispersion of pristine and acid-functionalized MWCNTs into the PI matrix, SEM measurements were performed on a cross-section of the composite films broken in liquid nitrogen. The bright dots and lines seen in SEM images (Figure 3) were attributed to the MWCNTs. It can be observed that the dispersion of MWCNTs in PI matrix is dependent on the type of the used filler; in all cases, MWCNTs-COOH has a higher degree of wrapping by the PI matrix as compared to the composites where pristine filler was introduced. Acid-functionalized MWCNTs promote an overall better interfacial interaction with PI matrix with no visible aggregation and a sufficient load transfer from the polymer matrix to the carbon nanotubes, except sample **cPI-Da**. This is consistent with the overall appearance of the composite films that showed homogeneous black colors, as can be seen in Figure 3. Instead, it is obvious from filament-like morphology of the samples **cPI-Ab**, **cPI-Bb**, **cPI-Cb** and **cPI-Db** that some of the nanotubes protuberate out of the polymer matrix and tend to agglomerate to some extent. Especially for the samples **cPI-Cb** and **cPI-Db**, alternate regions of agglomerated MWCNTs and “empty” PI matrix were identified, demonstrating the absence of proper interactions between pristine MWCNTs and the matrix. Overall, it can be concluded that method D involving thermal

imidization in a solution of PAA in the presence of MWCNT fillers is unfavorable towards homogeneous dispersions in this particular case of a CN-functionalized PI matrix.

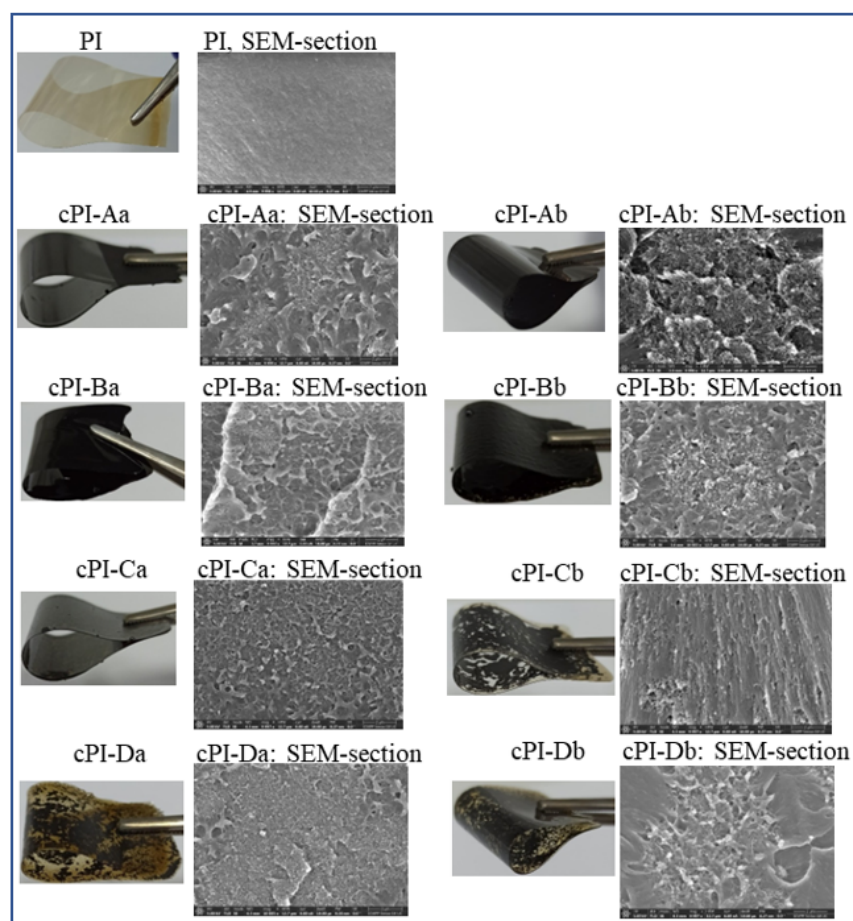


Figure 3. Photographs of PI matrix and all composite films in bended state and their SEM micrographs in cross-sections (2 μm surface, magnification of 10,000 \times).

3.3. Mechanical Properties

The tensile tests of the nanocomposite films incorporating 2 wt.% pristine or acid-functionalized MWCNTs offered a deeper insight in relation with the nature of MWCNTs inserted into the PI matrix. Although all free-standing PI reference and composite films were obtained by drop-casting a 12 wt.% polymer solution (PAA or PI solution, depending on the method) and 2 wt.% MWCNTs, the thicknesses of the films varied in the large interval of 45–90 μm due to the different distribution of the filler in the PI matrix. The initial visual observation of the reference and composite films during repeated bending enabled a first understanding of the mechanical behavior of the films, regardless of their homogeneity. As can be seen in Figure 3, the reference and the nanocomposite films incorporating 2 wt.% MWCNTs were flexible, tough and maintained their integrity at bending, demonstrating good resistance to mechanical stress.

Tensile tests performed on all samples enabled more quantitative evaluation with regard to their resistance to the applied stress (Table 1). The reference PI film matrix registered tensile strength and elongation at break values of 95.38 MPa and 9.45%, respectively. These values are comparable to those reported for related polyimide films derived from the same dianhydride and aromatic diamines incorporating ether groups without CN units, whose tensile strength and elongation at break values were found in the range of 102–107 MPa and 7–8%, respectively [45]. Unexpectedly, in the case of nanocomposite films, the incorporation of MWCNTs in the PI matrix led to a decrease in all measured

parameters. This behavior may be attributed to the insufficient or low physical interactions between the PI matrix and MWCNT fillers. Despite the acid-functionalization of MWCNTs, which led to a more homogeneous dispersion of the carbon nanotubes in the PI matrix, the measured mechanical parameters were inferior to those of the matrix, contrary to expectations. It seems that the interfacial adhesion of PI chains around the MWCNTs is not good enough to enable a strengthening between the two components, leading to lower mechanical features of the composites. Still, as mentioned earlier, the composite films displayed high mechanical resistance and maintained their integrity after several bendings, being suitable for use as advanced flexible materials.

The data obtained for each composite film parameter may be discussed in correlation with the applied method and the nature of MWCNTs. First, the series based on acid-functionalized MWCNTs was analyzed. The tensile strength values were higher for nanocomposites obtained by methods B and A (Table 1), indicating better mechanical resistance of composite films **cPI-Ba** and **cPI-Aa** compared to **cPI-Ca** and **cPI-Da** films. The elongation at break of **cPI-Aa** was slightly higher than for other acid-functionalized MWCNTs-based samples, which may suggest a more efficient interpenetration of MWCNTs between polyimide chains enabling an increased flexibility. As for nanocomposite films based on pristine MWCNTs, method A involving solid-state imidization in the presence of the fillers was the most appropriate for obtaining tougher films by providing a favorable environment for matrix–filler interactions even in the stage of PAA.

The results suggest that the optimal content of MWCNT loading for this PI matrix is less than 2 wt.%, since the expected increase in tensile tests did not occur. Similar reduction in mechanical properties of polyimides–carbon nanotube composites were found at filler loadings higher than 5 wt.% when the matrix incorporated functional groups able to develop interactions with the filler [31,47]. It may be possible that a certain degree of MWCNTs' re-aggregation occurred during the removal of the solvent and an incomplete wetting of MWCNTs by the PI led to their poor dispersion and lower tensile test parameters. This aspect is more evident in SEM images of nanocomposite films obtained by using pristine MWCNTs (Figure 3) where a reduced coverage of their surface by the PI matrix may be observed. Additional parameters which usually create mechanical issues include the deficiency of MWCNTs' orientation in the polymer matrix and insufficient load transfer due to the lack of interfacial adhesion [10,48].

Overall, in our case, the small reduction in tensile properties may be a result of the cumulative effects mentioned above where the presence of inhomogeneities in the composite material leads to stress concentration in polymer-rich regions that could initiate cracks at lower strains than in a homogeneous material, causing failure initiation at lower strain and stress levels [49].

3.4. Thermal Behavior

The evaluation of thermal stability was accomplished based on differential scanning calorimetry and thermogravimetric analyses, as shown in Table 1. The glass transition temperature for all nanocomposites films does not differ from that of PI matrix, proving that the incorporation of 2 wt.% pristine or acid-functionalized MWCNTs does not significantly alter the molecular entanglement of these PI chains.

The initial decomposition temperature, taken as 5% weight loss (T_5), revealed an improvement for all analyzed samples as compared to the PI matrix ($T_5 = 526$ °C). Higher values for T_5 were obtained for the more homogeneous composite films based on acid-functionalized MWCNTs: **cPI-Aa**, **cPI-Ba** and **cPI-Ca** (546 °C, 540 °C and 544 °C, respectively). The degradation mechanism followed the same trend for both PI matrix and the nanocomposite films, employing two decomposition steps. The first step of decomposition was attributed to the less stable ether linkages, while the second step was due to the scission of the main polymer chain. In the case of nanocomposite films, the first step of degradation started at slightly higher values compared to the PI matrix, suggesting that some of the PI ether groups may be involved in interactions with MWCNTs. Instead, the second step

occurred at almost the same values for all samples, regardless of the filler type, with a broad TG band profile, without a clear peak in some cases (**cPI-Ba** and **cPI-Ca**). As expected, the introduction of MWCNTs in the PI matrix increased the thermal stability and the char residue of all analyzed samples, which makes the present films suitable for applications that require stability to high temperatures. Figure 4 show the DSC and TG/DTG curves of the PI matrix and the nanocomposite samples.

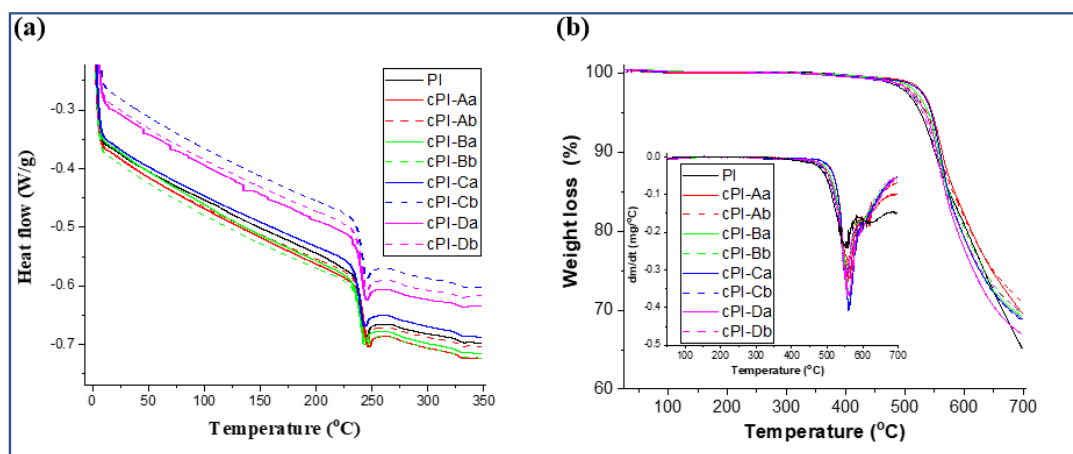


Figure 4. (a) DSC and (b) TG (DTG inset) curves of PI and the composites containing 2 wt.% MWCNTs.

3.5. Broadband Dielectric Spectroscopy (BDS) Study

It is generally known that the incorporation of MWCNTs into a polymer matrix leads to an enhancement of dielectric properties due to the localization of charges at the CNTs/polymer interfaces. This feature enables Maxwell–Wagner interfacial polarizations, when both real and imaginary permittivity of the composite material increases with MWCNT loading [50]. The registered BDS data of the nanocomposite films incorporating pristine MWCNTs were not discussed here since the agglomeration of the MWCNTs led to the formation of conductive channels with a high degree of conductivity that surpassed the measurement limits of the apparatus.

In the case of nanocomposite films incorporating acid-functionalized MWCNTs, typical examples of isothermal spectra showing the behavior of dielectric constant (ϵ') versus the external applied field frequency for **cPI-Aa** film are presented in Figure S2a. At low temperatures, between -100 °C and 0 °C, ϵ' decreases slowly with frequency increase, suggesting a low dipolar activity. At higher temperatures, however, the magnitude of ϵ' is considerably higher, especially at low frequencies, and sharply decreases with the further increase in frequency. The dispersion of ϵ' at low frequencies and the enhancement of ϵ' towards increasing temperatures are due to the occurrence of space-charge polarization. When the external electric field is applied, the space charges start to move and agglomerate at the contacts between the sample surfaces and electrodes used for dielectric spectroscopy measurements [51,52]. The latter effect is limited at low frequencies. At frequencies higher than 10^2 Hz, the electrode polarization-type signal diminished, revealing the intrinsic dipolar activity of the sample.

In Figure 5a, the $\epsilon'(f)$ spectra of PI matrix and the nanocomposites based on acid-functionalized MWCNTs at room temperature are comparatively displayed. Numerical values of ϵ' obtained at 100 Hz are presented in Table 2. As is common for polyimide-type films [53,54], ϵ' of PI matrix registered low values in the entire frequency range (e.g., at 100 Hz, ϵ' (PI) = 2.8). In the case of nanocomposite films, the effect of space-charge polarization is already detected at low frequencies, due to the incorporation of MWCNTs-COOH fillers. For **cPI-Ca** and **cPI-Da**, huge fluctuations in ϵ' were recorded due to increased conductivity and the distribution of MWCNTs around the percolation threshold. Therefore, we may assume that, at low frequencies, the dielectric constant of

the nanocomposite films is assisted by the presence of charge carriers injected through the incorporation of MWCNTs in the polyimide matrix.

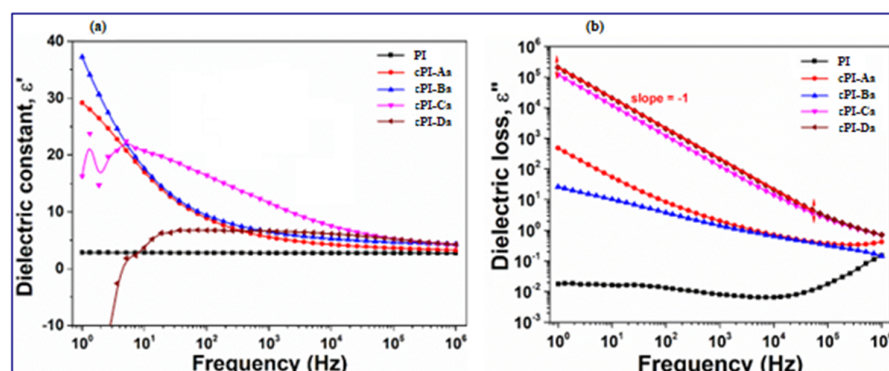


Figure 5. The evolution of (a) dielectric constant at room temperature for PI matrix and **cPI-Aa**, **cPI-Ba**, **cPI-Ca** and **cPI-Da** nanocomposites, and (b) comparative dielectric loss at room temperature for PI matrix and **cPI-Aa**, **cPI-Ba**, **cPI-Ca** and **cPI-Da** nanocomposites. In (b), the linear decrease tendency of ϵ'' with frequency was evaluated with a linear fit function.

The variation of dielectric loss, ϵ'' , with frequency increase is shown in Figure S2b for **cPI-Ba** film at various temperatures. Overall, ϵ'' decreases gradually with increasing frequency, and the magnitude of ϵ'' exhibits a slight enhancement when the temperature is varied between $-100\text{ }^{\circ}\text{C}$ and $250\text{ }^{\circ}\text{C}$. Following Figure 5b, the smallest dielectric loss is recorded for the neat polyimide in the entire frequency range. On the other hand, the magnitude of dielectric loss considerably grows for the nanocomposites with 2 wt.% acid-functionalized MWCNTs. The numerical values of ϵ'' obtained at 100 Hz and various temperatures are listed in Table 2. It may be noticed that, in the cases of **cPI-Ca** and **cPI-Da**, the dielectric loss reveals a linear drop in its magnitude towards increasing frequency. According to the published information, a decreasing tendency obtained in the double logarithmic plot with a slope close to -1 suggests the existence of electric charges in the material [55]. The latter behavior is detected in a wide spectral region, between 10^0 Hz and 10^4 Hz, revealing that the signal of long-range charge carriers is dominant and covers the dipolar relaxations of the material.

Table 2. Numerical values of dielectric constant, dielectric loss and conductivity obtained at 100 Hz and various temperatures.

Sample	Dielectric Constant, ϵ'			Dielectric Loss, ϵ''			Conductivity, σ (S/cm)		
	$-100\text{ }^{\circ}\text{C}$	$25\text{ }^{\circ}\text{C}$	$200\text{ }^{\circ}\text{C}$	$-100\text{ }^{\circ}\text{C}$	$25\text{ }^{\circ}\text{C}$	$200\text{ }^{\circ}\text{C}$	$-100\text{ }^{\circ}\text{C}$	$25\text{ }^{\circ}\text{C}$	$200\text{ }^{\circ}\text{C}$
PI	2.7	2.8	3.1	0.002	0.01	0.04	1.4×10^{-13}	7.4×10^{-13}	2.3×10^{-12}
cPI-Aa	7.4	8.9	12.9	4.8	8.4	18.7	2.7×10^{-10}	4.7×10^{-10}	1×10^{-9}
cPI-Ba	8.3	9.4	11.7	2.8	3.8	5.8	1.5×10^{-10}	2.1×10^{-10}	3.2×10^{-10}
cPI-Ca	14.8	16.4	20.4	703	1217	1854	3.9×10^{-8}	6.8×10^{-8}	1×10^{-7}
cPI-Da	6.5	6.7	7.3	1436	2068	3002	8×10^{-8}	1.1×10^{-7}	1.7×10^{-7}

The representative isothermal plots of conductivity, σ , as function of frequency at selected temperatures are presented for **cPI-Ca** in Figure S3a. The $\sigma(f)$ spectra encloses two different regimes: the first one is observed at low frequencies as a plateau region of conductivity, independent by frequency, that is generally assigned to the transport of free charges over long distances. The second regime is limited at high frequencies and is expressed as a gradual increase in conductivity with the raise of frequency. The latter may be attributed to the short-range charge fluctuations or the bound charges from the

material [56]. The flat region of conductivity is correlated with the drop in the dielectric constant and the linear decrease in dielectric losses, confirming the existence of free electric charges. As presented in Figure 6a, the frequency dependence of conductivity of PI matrix displays a capacitive behavior, which is typical for insulators. On the other hand, the $\sigma(f)$ profiles for **cPI-Ca** and **cPI-Da** are dominated by a resistive behavior, limited around 10^{-7} S/cm, that originates from the free charge carriers moving through the polymer lattice.

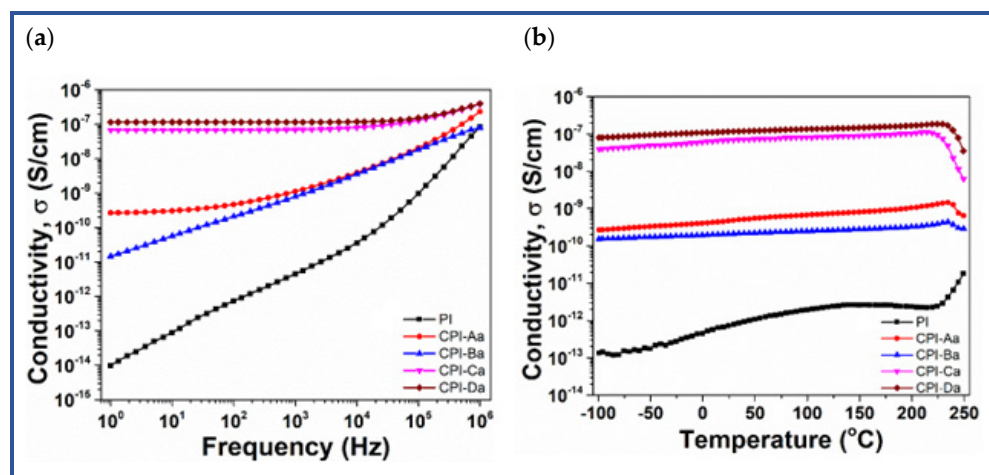


Figure 6. The evolution of conductivity (a) for PI matrix and **cPI-Aa**, **cPI-Ba**, **cPI-Ca** and **cPI-Da** nanocomposites at room temperature, and (b) as function of temperature at 100 Hz for PI matrix and **cPI-Aa**, **cPI-Ba**, **cPI-Ca** and **cPI-Da** nanocomposites.

The evolution of conductivity with temperature at various frequencies is represented for **cPI-Da** in Figure S3b. The moderate increase in conductivity increasing temperature reveals a good thermal stability of the sample. The broad band detected above 200 °C (e.g., at $f = 1$ Hz, the broad band is centered around 225 °C) may be assigned with the glass transition temperature of **cPI-Da**. There is a slight difference between the values of T_g registered by the two methods, BDS and DSC, that may be attributed to the particular experimental setups of each apparatus. The magnitude of σ is considerably enlarged at 10^5 Hz and 10^6 Hz, as previously observed in Figure S3a and Figure 6a. The isochronal plots of conductivity as function of temperature are comparatively depicted in Figure 6b for PI matrix and nanocomposites based on acid-functionalized MWCNTs. The $\sigma(T)$ profiles of nanocomposites exhibit a similar pattern: a slight increase in conductivity between -100 °C and 200 °C, followed by a significant decrease above T_g . Instead, for the PI matrix, an intense increase in σ occurred at the glass transition. The conductivity of nanocomposites is noticeably enhanced, as compared with that of the PI reference. Hereafter, the conductivity of **cPI-Aa** and **cPI-Ba** was around 10^{-10} S/cm, while **cPI-Ca** and **cPI-Da** registered σ values between 10^{-8} S/cm and 10^{-7} S/cm (Table 2).

Overall, **cPI-Aa** and **cPI-Ba** films can be acknowledged between high k dielectric materials with low dielectric loss with potential for use in field-effect transistors or thin film capacitors.

3.6. Energy Storage Ability of *cPI*-MWCNTs Flexible Electrodes

Carbonaceous materials such as carbon nanotubes are promising materials for use as electrodes in electrical double-layer capacitors (EDLCs) due to their high surface area, good conductivity and low cost. Although multi-walled carbon nanotubes (MWCNTs) displayed capacitance ranging from 4 to 135 F/g, they have the great inconvenience of inhomogeneous dispersion in pristine form in any solvent when they tend to agglomerate. A viable solution to this problem is represented by the functionalization of carbon nanotubes, or their mixing with polymers or metal oxides, which enables an increase in the capacitance [57]. Therefore, it appears to us of particular interest to explore the electrode behavior of the synthesized

PI nanocomposites and to assess their electrical charge storage capability. To this aim, both cyclic voltammetry (CV) and galvanostatic charge–discharge (GCD) measurements in a three-electrode cell configuration were carried out with the obtained free-standing films as electrode materials. From the library of the eight developed composite films, only five with homogeneous dispersion of MWCNTs were selected for measurements. The initial screening performed by CVs on **cPI-Aa**, **cPI-Ab**, **cPI-Ba**, **cPI-Bb** and **cPI-Ca** samples in different electrolyte systems (0.1 M TBAP/ACN, 0.1 M LiClO₄/ACN and 0.5 M KCl_{aq}) showed that only **cPI-Ab** based on pristine MWCNTs and **cPI-Ca** based on acid-functionalized MWCNTs have potential for electrical charge storage, the other samples providing too low currents (in the nA range) for conclusive results. Therefore, these two samples were further employed in detailed electrochemical studies, and the obtained results are discussed as follows.

3.6.1. CV Investigations

cPI-Ca and **cPI-Ab** nanocomposite free-standing films were investigated by using cyclic voltammetry (CV) experiments in a classical three-electrode cell configuration with the free-standing composite film as the working electrode and Pt wire as the counter electrode. The CV curves were registered both in organic (LiClO₄ or TBAP/ACN, 0.1 M solution) and aqueous (KCl/H₂O, 5 M solution) electrolytes at different potential scan rates between 20 and 500 mV/s in order to evaluate the best medium for charge storage. The optimum potential window was established for each sample after multiple CV scans in different potential domains until a near-rectangular pattern of the CV diagram was obtained at 20 mV/s, overall between −1.5 V and 1.1 V, against the standard Ag/Ag⁺ electrode. Since no redox activity was noticed for the CN-based PI matrix, the charge storage is presumed to occur on the basis of the electric double-layer capacitive (EDLC) mechanism.

Thus, for the nanocomposite based on 2 wt.% acid-functionalized MWCNTs obtained by the templated polycondensation method (**cPI-Ca**), the achieved currents in organic and aqueous electrolyte solutions had low values in the range of 10^{−9} A. According to the CV profiles of the investigated electrodes registered at scan rates between 20 and 500 mV/s, we have concluded that the charge storage capability of **cPI-Ca** is poor, although expected due to the low content of MWCNTs in the sample and its modest conductivity, in addition to dense structure of the PI matrix, which together promote low adsorption and transport of the electrolyte ions. To simulate the capacitive behavior of this sample at higher loading of MWCNTs, the carbon content was increased by applying a uniform layer of carbon paste on one surface of the composite film (sample denoted as **cPI-Ca/C paste**). The CV measurements carried out on this flexible electrode evidenced significantly higher currents in both electrolytes of about 10^{−6} A and 10^{−4} A in the organic and aqueous electrolyte, respectively, which suggested a better charge-storage capability of this material.

The specific gravimetric capacitance ($C_{m,CV}$, F/g) was estimated from CV curves according to the relation:

$$C_{m,CV} = \frac{\int I(V)dV}{2\Delta Vmv}$$

where $\int I(V)dV$ is the area of the CV curve, m is the mass of the electrode material, ΔV is the potential window set to record the CV curve and v is the scan rate. The $C_{m,CV}$ value obtained for the **cPI-Ca** sample at 20 mV/s was about 0.934 and 0.798 $\mu\text{F/g}$ in organic and aqueous electrolytes, respectively. The increase in the carbon content from **cPI-Ca/C paste** sample led to $C_{m,CV}$ values ranging from 5.581 mF/g to 0.127 mF/g in LiClO₄/ACN electrolyte solution and from 0.689 F/g to 0.048 F/g in aqueous solution, respectively, when the scan rate varied from 20 mV/s to 500 mV/s (Figure 7). According to these data, it can be stated that the increase in MWCNT loading in the chosen PI matrix beyond 2% may provide straightforward, flexible electrodes for high-performance, low-cost supercapacitors.

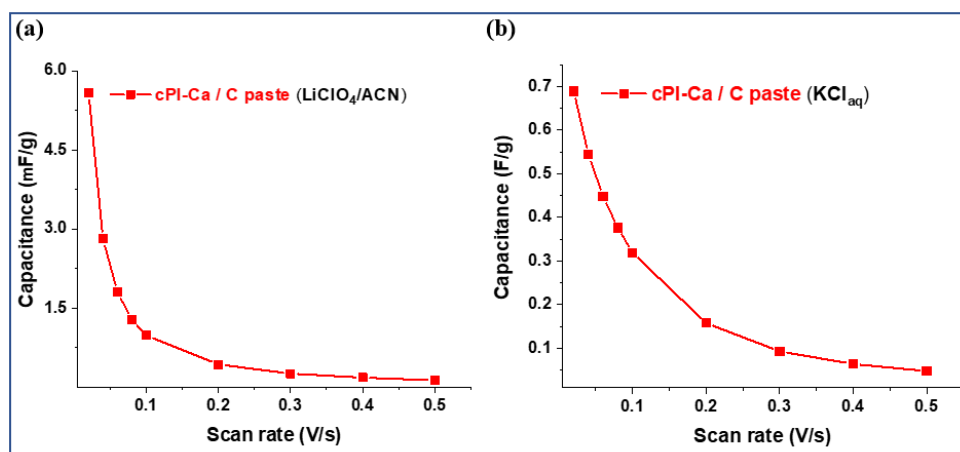


Figure 7. Evolution of specific gravimetric capacitance with scan rate for **cPI-Ca/C paste** sample in (a) $\text{LiClO}_4/\text{ACN}$ and (b) $\text{KCl}/\text{H}_2\text{O}$ electrolytes.

The rate capacity of the sample **cPI-Ab** obtained by the synthetic procedure detailed in Method A, where the PI matrix was loaded with 2 wt.% pristine MWCNTs, proved to be significantly different from the ones obtained for the **cPI-Ca** sample. The shape of the CV curves was almost rectangular in both electrolyte solutions, thus indicating the presence of a diffusion-controlled mechanism in this material, while the current reached 10^{-7} range (Figure 8a,b). The specific gravimetric capacitance as a function of the scan rate for **cPI-Ab** free-standing film measured in both organic and aqueous electrolytes is plotted in Figure 8c,d.

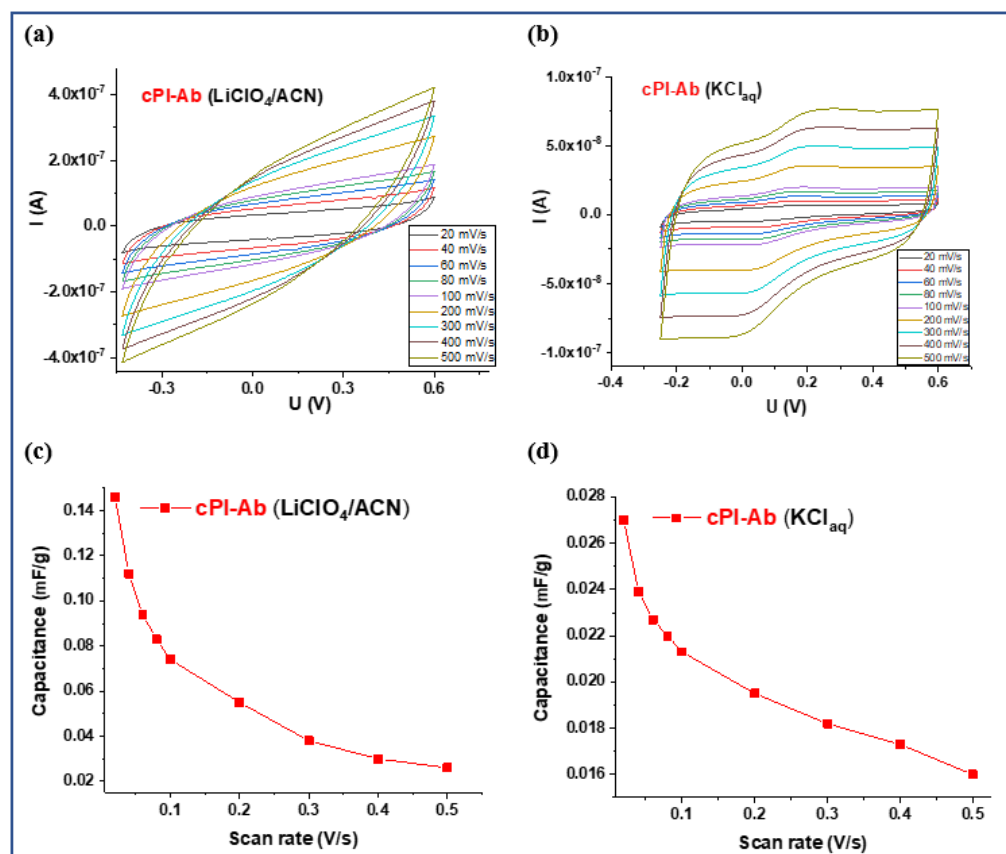


Figure 8. CV curves of **cPI-Ab** in (a) $\text{LiClO}_4/\text{ACN}$ and (b) 5M KCl aq at different scan rates. Evolution of specific gravimetric capacitance with scan rate in (c) $\text{LiClO}_4/\text{ACN}$ and (d) 5 M KCl aq.

The overall specific gravimetric capacitance decreased with the scan rate from 0.146 mF/g (at 20 mV/s) to 0.026 mF/g (at 500 mV/s) in LiClO₄/ACN electrolyte solution and from 0.027 mF/g (at 20 mV/s) to 0.016 mF/g (at 500 mV/s) in KCl aqueous solution. It is obvious that the capacitance values are considerably higher than those of the **cPI-Ca** film, most likely due to increased conductivity and higher surface areas of pristine MWCNTs compared to acid-functionalized MWCNTs which lost some of these properties. Generally, a series of defects arose after MWCNT functionalization, which reduced the electrical performance of the MWCNTs and, hence, the efficiency of their charge storage capacity, as is the case of the **cPI-Ca** sample. Accordingly, **cPI-Ab** shows promising potential for use as capacitive electrodes in flexible, low-cost supercapacitors.

However, to improve the electrical charge storage ability of this composite flexible electrode, an increase in the carbon content was considered as in the case of the **cPI-Ca** sample by painting one of the composite film surfaces with a thin layer of C paste. The rate capability of this electrode (**cPI-Ab/C paste**) was measured in KCl_{aq} electrolyte. As expected, the currents (Figure 9a) were considerably higher, whereas a three-orders-of-magnitude increase in the specific gravimetric capacitance was obtained, with the highest value of 0.149 F/g at 20 mV/s (Figure 9b).

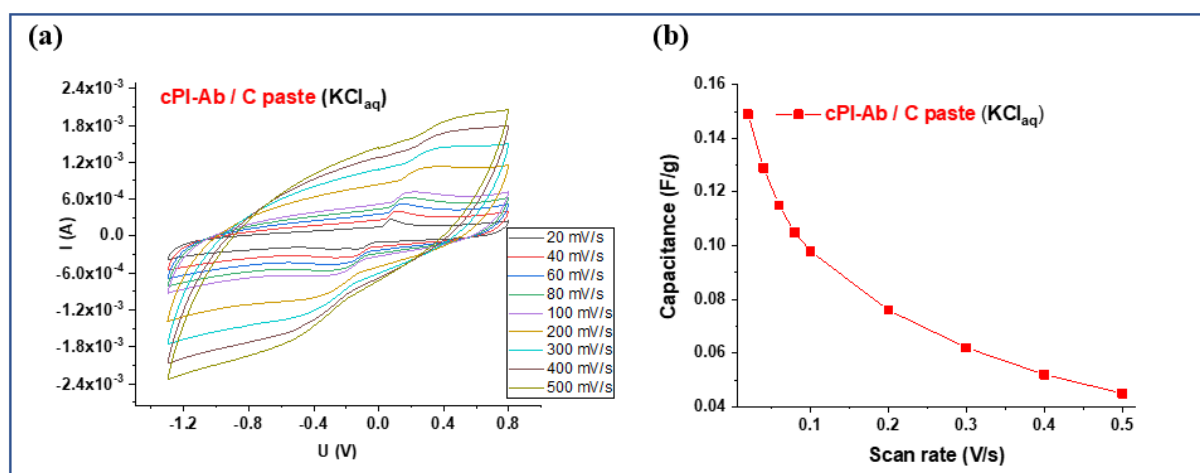


Figure 9. CV curves (a,b) specific gravimetric capacitance of **cPI-Ab/C paste** sample at different scan rates in KCl_{aq} electrolyte.

3.6.2. GCD Measurements

Galvanostatic charge–discharge (GCD) studies were further used to survey the charge storage capacity of the investigated **cPI-Ca** and **cPI-Ab** free-standing composite film electrodes. The charging–discharging process in a three-electrode configuration with both organic (TBAP/ACN) and aqueous (KCl/H₂O) electrolyte solutions took place at different current densities, depending on the sample and the selected electrolyte solution.

The voltage accumulated in the electrodes beyond which no further charging is possible, known as saturation charge voltage (V_{sc}) [58,59], was measured. After the saturation potential is achieved, the electrode begins the discharge process. In the case of the **cPI-Ca** sample, the GCD investigations evidenced very fast charge and discharge processes, a result in line with the low capacity to store charges assessed by CVs. Since **cPI-Ca/C paste** proved to be very efficient for this purpose, GCD measurements were also recorded on this sample. The V_{sc} value reached by this electrode was higher in the organic electrolyte (TBAP/ACN, 2.1 V) compared to the 1.4 V obtained in the KCl aqueous electrolyte. Furthermore, V_{sc} registered higher values at increased current densities. Figure 10 illustrates the GCD curves for **cPI-Ca/C paste** at different current densities selected according to the rate capability in the tested electrolyte (TBAP/ACN and KCl_{aq}). The charge–discharge behavior of this electrode at various time intervals until full charging in the organic electrolyte at a current density of 0.01/cm² is shown in Figure 10c.

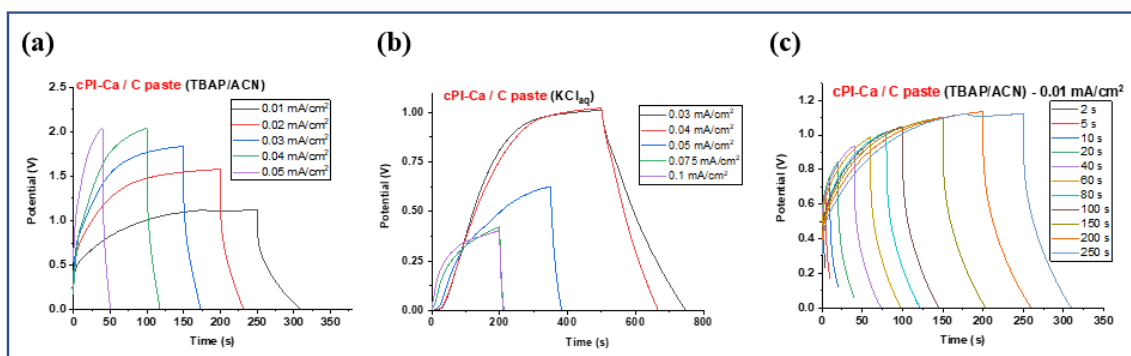


Figure 10. GCD curves of **cPI-Ca/C paste** at different current densities in (a) TBAP/ACN, (b) KCl_{aq}, and (c) different times until full charging in TBAP/ACN, at a current density of 0.01/cm².

The specific areal capacitance $C_{a,GCD}$ at different current densities was calculated according to the formula:

$$C_{a,GCD} = \frac{I \times \Delta t}{\Delta V \times a}$$

where I is the discharge current, Δt is the discharge time, ΔV is the operational potential (0 to V_{sc}) and a is the electrode area. The $C_{a,GCD}$ results obtained for the **cPI-Ca/C paste** sample were in the range of 5.09–1.57 mF/cm² at 0.01–0.05 mA/cm² and 17.38–0.16 mF/cm² at 0.03–0.1 mA/cm² in the organic and aqueous electrolytes, respectively. Thus, the maximum value of this parameter (17.38 mF/cm²) was registered at 0.03 mA/cm² in KCl aqueous electrolyte, being slightly higher than those reported for the related polyimide electrode containing 10 wt.% unmodified MWCNTs layered by C paste (2.64 mF/cm² at 0.025 mA/cm² in TBAF/PMMA electrolyte) which was successfully tested as an electrode material in flexible supercapacitors [31].

When **cPI-Ab** electrode was involved in GCD studies, similar results were obtained. Thus, by testing it in the pristine form in the three-electrode cell configuration, a poor operation capability was noticed due to rapid discharge processes, with specific areal capacitance varying from 0.118 to 0.053 μ F/cm² at current densities between 0.016 and 0.05 μ A/cm² in KCl aqueous electrolyte. Considerably higher electrical storage capability was obtained by the **cPI-Ab/C paste** electrode, demonstrated by the calculated $C_{a,GCD}$ values which were in the range of 16.03–14.71 mF/cm² at current densities between 20 and 50 μ A/cm² (Figure 11).

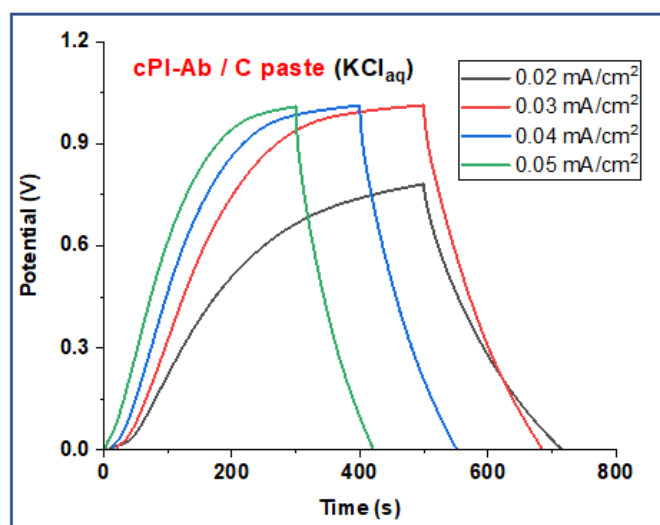


Figure 11. GCD curves of **cPI-Ab/C paste** in KCl_{aq} electrolyte at different current densities.

Overall, the data reported in this study emphasize that the synergistic effect of carbonaceous materials and PI matrix can be a feasible approach towards low-cost and flexible electrodes for supercapacitors. Since large specific surface area of MWCNTs enables electrolyte ions' adsorption on one hand, and the flexibility and toughness of the PIs provide an appropriate medium for their homogeneous dispersion on the other hand, these materials may work together towards satisfactory charge storage capability.

4. Conclusions

In order to obtain new composite materials for energy storage applications, a nitrile-containing polyimide with bulky fluorene units, 2 wt.% pristine or acid-functionalized MWCNTs and four synthetic pathways were employed towards developing flexible nanocomposite films. The polyimide matrix and the nanocomposites incorporating 2 wt.% pristine or acid-functionalized MWCNTs were characterized by means of morphology, mechanical, thermal and dielectric properties. FTIR spectra of the polyimide nanocomposites revealed significant band broadening of the absorption band characteristics for the functional groups of the composites as a proof of the specific interaction of MWCNTs with aromatic nuclei and ether units of the polyimide matrix. Morphology studies revealed higher degree of homogeneity in the case of composites containing acid-functionalized MWCNTs. The mechanical properties of the free-standing flexible nanocomposite films showed a small reduction in tensile properties as compared to the polyimide matrix due to a certain degree of MWCNTs re-aggregation during the removal of the solvent and/or an incomplete wetting of MWCNTs by the polyimide. In terms of thermal stability, the nanocomposites exhibited an increase in the initial decomposition temperature regardless of the nature of the filler compared to the matrix, while the glass transition temperature registered similar values for all samples. This suggests that no alteration in the molecular entanglement of these composite materials took place. Broadband dielectric studies evidenced increased dielectric constants (up to 14.8) for the nanocomposites when compared to the polyimide matrix, leading to materials with high k dielectric and low dielectric loss. Among the studied composites, only two of them showed promising results for use as flexible electrode materials in supercapacitors. Thus, the incorporation of pristine MWCNTs in polyimide matrix led to a better capacitance (0.146 mF/g for the **cPI-Ab** sample obtained from Method A) compared to acid-functionalized MWCNTs (0.934 μ F/g for the **cPI-Ca** sample obtained from Method C) at 20 mV/s in LiClO₄/acetonitrile electrolyte. To improve the electrical charge storage ability of these flexible electrodes, the composite films' surface was painted with a thin layer of C paste, achieving considerably higher electrical storage capability. The maximum value of specific areal capacitance obtained for the **cPI-Ca/C paste** sample (17.38 mF/cm² at 0.03 mA/cm²) was slightly higher than the **cPI-Ab/C paste** sample (16.03 mF/cm² at 0.02 mA/cm²) in KCl aqueous electrolyte. Overall, the data reported in this study emphasize that the synergistic effect of MWCNTs and polyimide matrix can be a successful approach towards low-cost and flexible electrode materials for supercapacitors.

Supplementary Materials: The following supporting information can be downloaded at: <https://www.mdpi.com/article/10.3390/en16093739/s1>, Figure S1: Photographs of the polyimide and of all composite films taken by optical microscopy (OM) at a magnification of 40 \times ; Figure S2: The evolution of (a) dielectric constant as function of frequency for **cPI-Aa** nanocomposite at various temperatures and of (b) dielectric loss as function of frequency for **cPI-Ba** nanocomposite at various temperatures; Figure S3: The evolution of conductivity as (a) function of frequency for **cPI-Ca** nanocomposite at various temperatures, and (b) function of temperature for **cPI-Da** nanocomposite at various frequencies.

Author Contributions: Conceptualization, I.B. and M.-D.D.; Data curation, A.P.C., M.A. and I.B.; Formal analysis, A.P.C., M.A. and D.R.; Investigation, A.P.C., M.A., D.R. and I.B.; Project administration, I.B.; Writing—original draft, A.P.C., M.-D.D. and I.B.; Writing—review and editing, I.B. and M.-D.D. All authors have read and agreed to the published version of the manuscript.

Funding: This work was supported by a grant of the Ministry of Research, Innovation and Digitization, CNCS—UEFISCDI, project number PN-III-P1-1.1-TE-2021-1110, within PNCDI III.

Data Availability Statement: Not applicable.

Conflicts of Interest: The authors declare no conflict of interest.

References

1. Yuan, D.; Zhu, Y.G.; Jia, C. Carbon nanotube—Polymer composites for energy storage applications. In *Carbon Nanotubes—Current Progress of Their Polymer Composites*; Berber, M.R., Hafez, I.H., Eds.; IntechOpen: London, UK, 2016. [CrossRef]
2. Simon, P.; Gogotsi, Y. Capacitive energy storage in nanostructured carbon–electrolyte systems. *Acc. Chem. Res.* **2012**, *46*, 1094–1103. [CrossRef] [PubMed]
3. Li, L.; Wu, Z.; Yuan, S.; Zhang, X. Advances and challenges for flexible energy storage and conversion devices and systems. *Energy Environ. Sci.* **2014**, *7*, 2101–2122. [CrossRef]
4. Niu, Z.; Liu, L.; Zhang, L.; Zhou, W.; Chen, X.; Xie, S. Programmable nanocarbon-based architectures for flexible supercapacitors. *Adv. Energy Mater.* **2015**, *5*, 1500677. [CrossRef]
5. Zhu, Y.G.; Wang, Y.; Shi, Y.; Wong, J.I.; Yang, H.Y. CoO nanoflowers woven by CNT network for high energy density flexible micro-supercapacitor. *Nano Energy* **2014**, *3*, 46–54. [CrossRef]
6. Zheng, S.; Zhang, J.; Deng, H.; Du, Y.; Shi, X. Chitin derived nitrogen-doped porous carbons with ultrahigh specific surface area and tailored hierarchical porosity for high performance supercapacitors. *J. Bioresour. Bioprod.* **2021**, *6*, 142–151. [CrossRef]
7. Yan, B.; Feng, L.; Zheng, J.; Zhang, Q.; Jiang, S.; Zhang, C.; Ding, Y.; Han, J.; Chen, W.; He, S. High performance supercapacitors based on wood-derived thick carbon electrodes synthesized via green activation process. *Inorg. Chem. Front.* **2022**, *9*, 6108–6123. [CrossRef]
8. Xiao, J.; Li, H.; Zhang, H.; He, S.; Zhang, Q.; Liu, K.; Jiang, S.; Duan, G.; Zhang, K. Nanocellulose and its derived composite electrodes toward supercapacitors: Fabrication, properties, and challenges. *J. Bioresour. Bioprod.* **2022**, *7*, 245–269. [CrossRef]
9. Zhou, Y.; Zhou, X.; Ge, C.; Zhou, W.; Zhu, Y.; Xu, B. Branched carbon nanotube/carbon nanofiber composite for supercapacitor electrodes. *Mater. Lett.* **2019**, *246*, 174–177. [CrossRef]
10. Khan, W.; Sharma, R.; Saini, P. Carbon Nanotube—Based polymer composites: Synthesis, properties and applications. In *Carbon Nanotubes—Current Progress of Their Polymer Composites*; Berber, M.R., Hafez, I.H., Eds.; IntechOpen: London, UK, 2016. [CrossRef]
11. Nalwa, H.S. (Ed.) *Handbook of Low and High Dielectric Constant Materials and Their Applications*; Academic Press/Harcourt Sci. & Tech. Co.: San Diego, CA, USA, 1999; Volume 2.
12. Ji, D.; Li, T.; Hu, W.; Fuchs, H. Recent progress in aromatic polyimide dielectrics for organic electronic devices and circuits. *Adv. Mater.* **2019**, *31*, 1806070. [CrossRef]
13. Hicyilmaz, A.S.; Bedeloglu, A.C. Applications of polyimide coatings: A review. *SN Appl. Sci.* **2021**, *3*, 363. [CrossRef]
14. Butnaru, I.; Chiriac, A.-P.; Tugui, C.; Asandulesa, M.; Damaceanu, M.-D. The synergistic effect of nitrile and jeffamine structural elements towards stretchable and high-k neat polyimide materials. *Mater. Chem. Front.* **2021**, *5*, 7558. [CrossRef]
15. Park, C.; Ounaies, Z.; Wise, K.E.; Harrison, J.S. In situ poling and imidization of amorphous piezoelectric polyimides. *Polymer* **2004**, *45*, 5417–5425. [CrossRef]
16. Bacosca, I.; Hamciuc, E.; Bruma, M. Effect of flexible linkages on the properties of poly(ether imide) films. *Soft Mater.* **2013**, *11*, 465–475. [CrossRef]
17. Butnaru, I.; Bruma, M.; Gaan, S. Phosphine oxide based polyimides: Structure–property relationships. *RSC Adv.* **2017**, *7*, 50508–50518. [CrossRef]
18. Wang, D.H.; Riley, J.K.; Fillery, S.P.; Durstock, M.F.; Vaia, R.A.; Tan, L.-S. Synthesis and characterization of unsymmetrical benzonitrile-containing polyimides: Viscosity-lowering effect and dielectric properties. *J. Polym. Sci. Part A Polym. Chem.* **2013**, *51*, 4998–5011. [CrossRef]
19. Treufeld, I.; Wang, D.H.; Kurish, B.A.; Tan, L.S.; Zhu, L. Enhancing electrical energy storage using polar polyimides with nitrile groups directly attached to the main chain. *J. Mater. Chem. A* **2014**, *2*, 20683–20696. [CrossRef]
20. Butnaru, I.; Constantin, C.-P.; Damaceanu, M.-D. Optimization of triphenylamine-based polyimide structure towards molecular sensors for selective detection of heavy/transition metal ions. *J. Photochem. Photobiol. A Chem.* **2023**, *435*, 114271. [CrossRef]
21. Kim, H.; Hwang, S.; Hwang, T.; Bin In, J.; Yeo, J. Digitally patterned mesoporous carbon nanostructures of colorless polyimide for transparent and flexible micro-supercapacitor. *Energies* **2021**, *14*, 2547. [CrossRef]
22. Saxena, A.; Prabhakaran, P.V.; Rao, V.L.; Ninan, K.N. Synthesis and characterization of polyamides and poly(amide-imide)s derived from 2,6-bis(3-aminophenoxy)benzotrile or 2,6-bis(4-aminophenoxy)benzotrile. *Polym. Int.* **2005**, *54*, 544–552. [CrossRef]
23. Li, L.; Kikuchi, R.; Kakimoto, M.-A.; Jikei, M.; Takahashi, A. Synthesis and characterization of new polyimides containing nitrile groups. *High Perform. Polym.* **2005**, *17*, 135–147. [CrossRef]
24. Bacosca, I.; Hamciuc, E.; Bruma, M.; Ronova, I.A. Study of aromatic polyimides containing cyano groups. *High Perform. Polym.* **2010**, *22*, 703–714. [CrossRef]
25. Basheer, B.V.; George, J.J.; Siengchin, S.; Parameswaranpillai, J. Polymer grafted carbon nanotubes—Synthesis, properties, and applications: A review. *Nano-Struct. Nano-Objects* **2020**, *22*, 100429. [CrossRef]

26. Yuen, S.M.; Ma, C.C.M.; Lin, Y.Y.; Kuan, H.C. Preparation, morphology and properties of acid and amine modified multiwalled carbon nanotube/polyimide composite. *Compos. Sci. Technol.* **2007**, *67*, 2564–2573. [[CrossRef](#)]
27. Chang, C.M.; Liu, Y.L. Functionalization of multi-walled carbon nanotubes with non-reactive polymers through an ozone-mediated process for the preparation of a wide range of high performance polymer/carbon nanotube composites. *Carbon* **2010**, *48*, 1289–1297. [[CrossRef](#)]
28. Chou, W.J.; Wang, C.C.; Chen, C.Y. Characteristics of polyimide-based nanocomposites containing plasma-modified multi-walled carbon nanotubes. *Compos. Sci. Technol.* **2008**, *68*, 2208–2213. [[CrossRef](#)]
29. Lin, W.; Moon, K.S.; Wong, C.P. A combined process of in situ functionalization and microwave treatment to achieve ultrasmall thermal expansion of aligned carbon nanotube–polymer nanocomposites: Toward applications as thermal interface materials. *Adv. Mater.* **2009**, *21*, 2421–2424. [[CrossRef](#)]
30. Huang, Y.C.; Lin, J.H.; Tseng, I.H.; Lo, A.Y.; Lo, T.Y.; Yu, H.P.; Tsai, M.H.; Whang, W.T.; Hsu, K.Y. An in situ fabrication process for highly electrical conductive polyimide/ MWCNT composite films using 2,6-diaminoanthraquinone. *Compos. Sci. Technol.* **2013**, *87*, 174–181. [[CrossRef](#)]
31. Butnaru, I.; Chiriac, A.-P.; Constantin, C.P.; Damaceanu, M.-D. Insights into MWCNTs/polyimide nanocomposites: From synthesis to application as free-standing flexible electrodes in low-cost micro-supercapacitors. *Mater. Today Chem.* **2022**, *23*, 100671. [[CrossRef](#)]
32. Govindaraj, B.; Sarojadevi, M. Microwave-assisted synthesis of nanocomposites from polyimides chemically cross-linked with functionalized carbon nanotubes for aerospace applications. *Polym. Adv. Technol.* **2018**, *29*, 1718–1726. [[CrossRef](#)]
33. Zindy, N.; Aumaitre, C.; Mainville, M.; Saneifar, H.; Johnson, P.A.; Bélanger, D.; Leclerc, M. Pyrene diimide based π -conjugated copolymer and single-walled carbon nanotube composites for lithium-ion batteries. *Chem. Mater.* **2019**, *31*, 8764–8773. [[CrossRef](#)]
34. Han, N.K.; Choi, Y.C.; Park, D.U.; Ryu, J.H.; Jeong, Y.G. Core-shell type composites based on polyimide-derived carbon nanofibers and manganese dioxide for self-standing and binder-free supercapacitor electrode applications. *Compos. Sci. Technol.* **2020**, *196*, 108212. [[CrossRef](#)]
35. Gao, W.; Zhang, Z.; Zhang, Y.; Ma, B.; Luo, J.; Deng, J.; Yuan, W. Efficient carbon nanotube/polyimide composites exhibiting tunable temperature coefficient of resistance for multi-role thermal films. *Compos. Sci. Technol.* **2020**, *199*, 108333. [[CrossRef](#)]
36. Wang, Y.-Y.; Zhou, Z.-H.; Zhou, C.-G.; Sun, W.-J.; Gao, J.-F.; Dai, K.; Yan, D.-X.; Li, Z.-M. Lightweight and robust carbon nanotube/polyimide foam for efficient and heat-resistant electromagnetic interference shielding and microwave absorption. *ACS Appl. Mater. Interfaces* **2020**, *12*, 8704–8712. [[CrossRef](#)] [[PubMed](#)]
37. Burç, M.; Köytepe, S.; Duran, S.T.; Ayhan, N.; Aksoy, B.; Seçkin, T. Development of voltammetric sensor based on polyimide-MWCNT composite membrane for rapid and highly sensitive detection of paracetamol. *Measurement* **2020**, *151*, 107103. [[CrossRef](#)]
38. Farahani, M.H.D.A.; Hua, D.; Chung, T.-S. Cross-linked mixed matrix membranes consisting of carboxyl-functionalized multi-walled carbon nanotubes and P84 polyimide for organic solvent nanofiltration (OSN). *Sep. Purif. Technol.* **2017**, *186*, 243–254. [[CrossRef](#)]
39. Jeong, Y.; Park, J.; Lee, J.; Kim, K.; Park, I. Ultrathin, biocompatible, and flexible pressure sensor with a wide pressure range and its biomedical application. *ACS Sens.* **2020**, *5*, 481–489. [[CrossRef](#)]
40. Li, X.; Jiang, Y.; Jia, L.; Wang, C. MoO₂ nanoparticles on reduced graphene oxide/polyimide-carbon nanotube film as efficient hydrogen evolution electrocatalyst. *J. Power Sources* **2016**, *304*, 146–154. [[CrossRef](#)]
41. Kang, J.H.; Park, C.; Lowther, S.E.; Harrison, J.S.; Park, C.E. All-organic actuator fabricated with single wall carbon nanotube electrodes. *J. Polym. Sci. Part B Polym. Phys.* **2008**, *46*, 2532–2538. [[CrossRef](#)]
42. Kang, J.H.; Park, C.; Gaik, S.J.; Lowther, S.E.; Harrison, J.S. The effect of single wall carbon nanotubes on the dipole orientation and piezoelectric properties of polymeric nanocomposites. *NANO Brief Rep. Rev.* **2006**, *1*, 77–85. [[CrossRef](#)]
43. Ounaies, Z.; Park, C.; Harrison, J.; Lillehei, P. Evidence of piezoelectricity in SWCNT polyimide and SWNT-PZT-polyimide composites. *J. Thermoplast. Compos. Mater.* **2008**, *21*, 393–409. [[CrossRef](#)]
44. Saito, T.; Matsushige, K.; Tanaka, K. Chemical treatment and modification of multi-walled carbon nanotubes. *Phys. B Condens. Matter* **2002**, *323*, 280–283. [[CrossRef](#)]
45. Hsiao, S.H.; Li, C.T. Synthesis and characterization of new fluorene-based poly(ether imide)s. *J. Polym. Sci. Part A Polym. Chem.* **1999**, *37*, 1403–1412. [[CrossRef](#)]
46. Bruma, M.; Damaceanu, M.D.; Muller, P. Comparative study of polyimides containing oxadiazole and ether groups. *High Perform. Polym.* **2009**, *21*, 522–534. [[CrossRef](#)]
47. Lebrón-Colón, M.; Meador, M.A.; Gaier, J.R.; Solá, F.; Scheiman, D.A.; McCorkle, L.S. Reinforced thermoplastic polyimide with dispersed functionalized single wall carbon nanotubes. *ACS Appl. Mater. Interf.* **2010**, *2*, 669–676. [[CrossRef](#)]
48. An, L.; Pan, Y.Z.; Shen, X.W.; Lu, H.B.; Yang, Y.L. Rod-like attapulgite/polyimide nanocomposites with simultaneously improved strength, toughness, thermal stability and related mechanisms. *J. Mater. Chem.* **2008**, *18*, 4928–4941. [[CrossRef](#)]
49. Misiego, C.R.; Pipes, R.B. Dispersion and its relation to carbon nanotube concentration in polyimide nanocomposites. *Compos. Sci. Technol.* **2013**, *85*, 43–49. [[CrossRef](#)]
50. Saini, P.; Choudhary, V.; Singh, B.P.; Mathur, R.B.; Dhawan, S.K. Enhanced microwave absorption behavior of polyaniline-CNT/polystyrene blend in 12.4–18.0 GHz range. *Synth. Met.* **2011**, *161*, 1522–1526. [[CrossRef](#)]
51. Kareem, A.A. Preparation and electrical properties of polyimide/carbon nanotubes composites. *Mater. Sci. Pol.* **2017**, *35*, 755–759. [[CrossRef](#)]

52. Asandulesa, M.; Kostromin, S.; Aleksandrov, A.; Tameev, A.; Bronnikov, S. The effect of PbS quantum dots on molecular dynamics and conductivity of PTB7:PC71BM bulk heterojunction as revealed by dielectric spectroscopy. *Phys. Chem. Chem. Phys.* **2022**, *24*, 9589–9596. [[CrossRef](#)]
53. Chisca, S.; Musteata, V.E.; Sava, I.; Bruma, M. Dielectric behavior of some aromatic polyimide films. *Eur. Polym. J.* **2011**, *47*, 1186–1197. [[CrossRef](#)]
54. Bei, R.; Qian, C.; Zhang, Y.; Chi, Z.; Liu, S.; Chen, X.; Xu, J.; Aldred, M.P. Intrinsic low dielectric constant polyimides: Relationship between molecular structure and dielectric properties. *J. Mater. Chem. C* **2017**, *5*, 12807–12815. [[CrossRef](#)]
55. Pochard, I.; Vall, M.; Eriksson, J.; Farineau, C.; Cheung, O.; Frykstrand, S.; Welch, K.; Stromme, M. Amine-functionalised mesoporous magnesium carbonate: Dielectric spectroscopy studies of interactions with water and stability. *Mater. Chem. Phys.* **2018**, *216*, 332–338. [[CrossRef](#)]
56. Asandulesa, M.; Musteata, V.E.; Bele, A.; Dascalu, M.; Bronnikov, S.; Racles, C. Molecular dynamics of polysiloxane polar-nonpolar co-networks and blends studied by dielectric relaxation spectroscopy. *Polymer* **2018**, *149*, 73–84. [[CrossRef](#)]
57. Aboutalebi, S.H.; Chidembo, A.T.; Salari, M.; Konstantinov, K.; Wexler, D.; Liu, H.K.; Dou, S.X. Comparison of GO, GO/MWCNTs composite and MWCNTs as potential electrode materials for supercapacitors. *Energy Environ. Sci.* **2011**, *4*, 1855–1865. [[CrossRef](#)]
58. Zhang, S.; Pan, N. Supercapacitors performance evaluation. *Adv. Energy Mater.* **2015**, *5*, 1401401. [[CrossRef](#)]
59. Manjakkal, L.; Navaraj, W.T.; Núñez, C.G.; Dahiya, R. Graphene–graphite polyurethane composite based high-energy density flexible supercapacitors. *Adv. Sci.* **2019**, *6*, 1802251. [[CrossRef](#)] [[PubMed](#)]

Disclaimer/Publisher’s Note: The statements, opinions and data contained in all publications are solely those of the individual author(s) and contributor(s) and not of MDPI and/or the editor(s). MDPI and/or the editor(s) disclaim responsibility for any injury to people or property resulting from any ideas, methods, instructions or products referred to in the content.